

Electronic Supplementary Information (ESI) for

Organic-Inorganic Macroion Coacervate Complexation

Benxin Jing,[†] Jie Qiu,[‡] and Yingxi Zhu^{†,*}

[†]Department of Chemical Engineering and Materials Science, Wayne State University, Detroit, Michigan 48202

[‡]Department of Civil, Environmental Engineering and Earth Sciences, University of Notre Dame, Notre Dame, IN
46556

*Corresponding Author: yzhu3@wayne.edu.

1. *Morphological Structure and Liquid-like Behavior of PSBMA- $\{W_{12}\}$ Coacervates.*

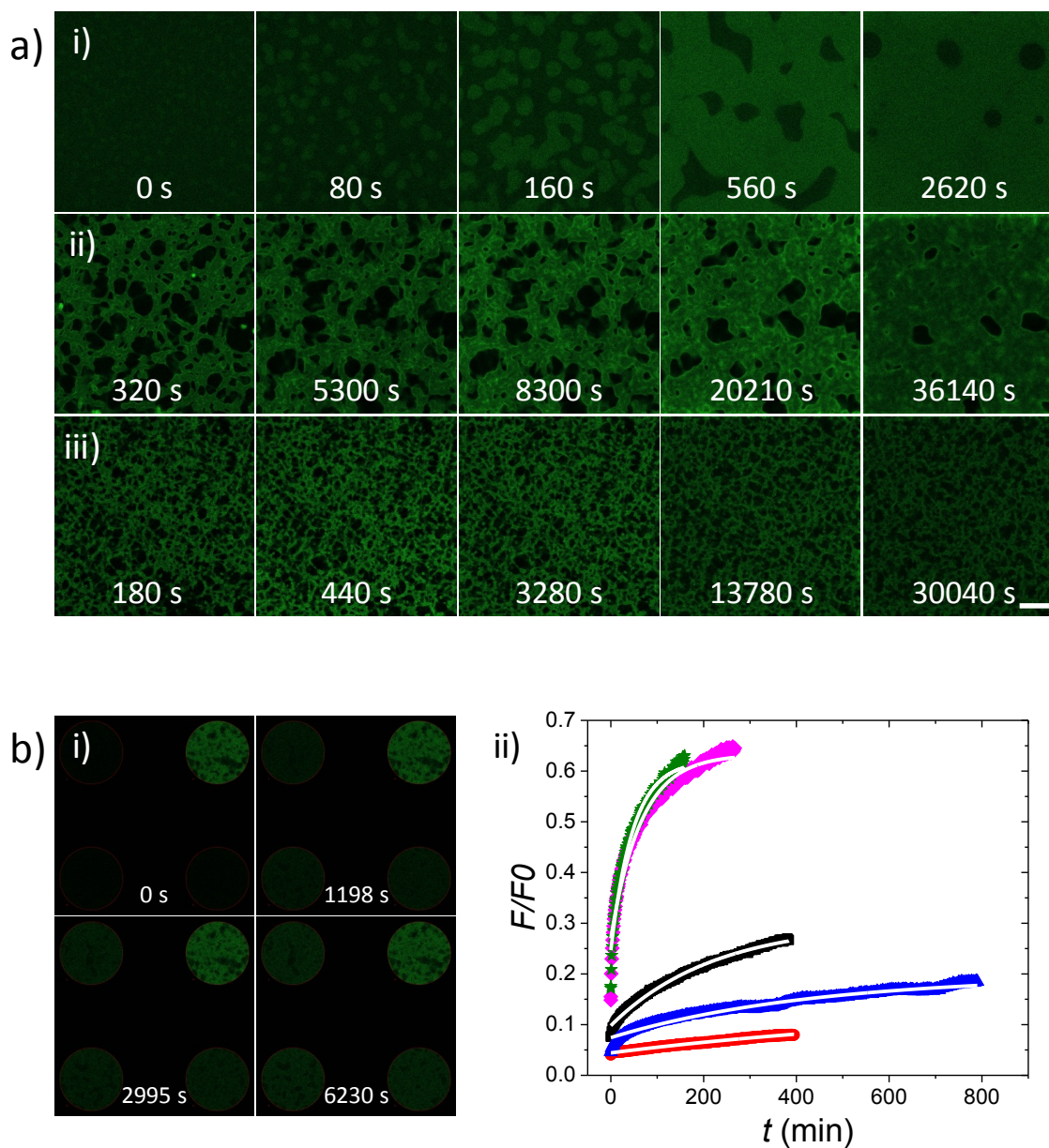


Figure S1. a) Time (t)-dependent morphological structure of PSBMA- $\{W_{12}\}$ complexes formed at constant PSBMA concentration, $c_{SBMA} = 85.5$ mM and LiCl concentration, $c_{LiCl} = 0.5$ M at varied $c_{e-\{W_{12}\}}/c_{SBMA} =$ i) 80%, ii) 120%, and iii) 160%. Elapsed time after mixing is noted in each fluorescence micrograph. The scale bar is 20 μm . b)-i) Representative fluorescence micrographs exhibit the fluorescence recovery after photobleaching of matured PSBMA- $\{W_{12}\}$ coacervates formed at $c_{SBMA} = 85.5$ mM, $c_{LiCl} = 0.5$ M, and $c_{e-\{W_{12}\}}/c_{SBMA} = 200\%$. Three circular areas of diameter, $d = 32$ μm are bleached and recorded in comparison to one unbleached circular area of the same diameter as the reference. ii) Time-dependent fluorescence recovery profiles of the coacervates formed at $c_{e-\{W_{12}\}}/c_{SBMA} = 80\%$ (black squares), 120%

(red circles), 160% (blue triangles), 200% (magenta diamonds), and 220% (olive stars). All the data are acquired with the samples matured one week after initial mixing, when the morphology of the coacervates change little with further elapsed time. Time-dependent fluorescence intensity, $F(t)$, normalized by that of the unbleached region, $F(0)$ is fitted by one-phase exponential function (white lines) by using the “Bottom to (Span + Bottom)” analysis: $F(t)/F(0) = Bottom + Span * (1 - \exp(-t \ln 2 / \tau_{1/2}))$, where $\tau_{1/2}$ is the half-time for diffusion^{1,2}. Thereby the apparent diffusion coefficient of coacervates in aqueous media is obtained from $\tau_{1/2}$ according to $D = d^2 / (4\tau_{1/2})$ as $0.028 \mu\text{m}^2/\text{s}$, $0.0076 \mu\text{m}^2/\text{s}$, $0.014 \mu\text{m}^2/\text{s}$, $0.095 \mu\text{m}^2/\text{s}$, and $0.13 \mu\text{m}^2/\text{s}$ corresponding to $c_{e-(W12)}/c_{SBMA} = 80 \%$, 120% , 160% , 200% , and 220% , respectively.

2. Generality of PSBMA-POM Coacervate Complexation with Different POMs.

The generality of PSBMA-POM coacervation was confirmed with other POM anions of similar atomic architecture structure but varied charge valence and size, including $\{\text{SiW}_{12}\}^{4-}$, $\{\text{PW}_9\}^{9-}$, $\{\text{Ni}_9\}^{16-}$. Similar phase behavior with dependence on the molar ratio of total POM charge concentration to total SBMA monomer concentration is observed in **Figure S2**. Silicotungstic acid ($\{\text{SiW}_{12}\}^{4-}$) was purchased from Sigma-Aldrich and used directly. $\text{Na}_9\text{PW}_9\text{O}_{34}$ ($\{\text{PW}_9\}^{9-}$) and $\text{K}_5\text{Na}_{11}[\text{Ni}_9(\text{OH})_3(\text{H}_2\text{O})_6(\text{HPO}_4)_2(\text{PW}_9\text{O}_{34})_3]$ ($\{\text{Ni}_9\}^{16-}$) were synthesized by strictly following the published procedure.^{3,4}

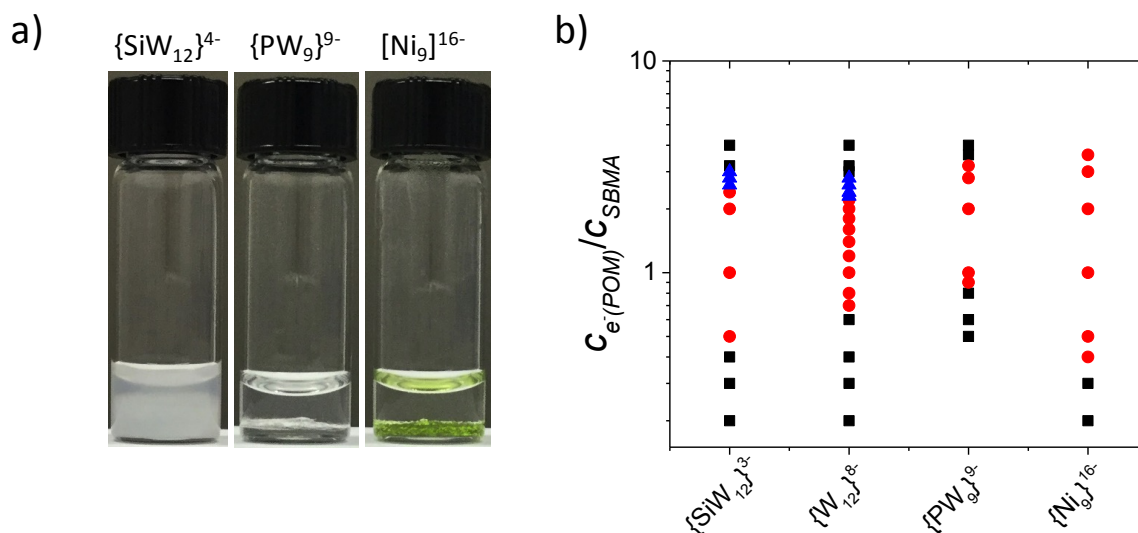


Figure S2. a) Photographs show the formation of biphasic coacervate complexes of PSBMA with $\{\text{SiW}_{12}\}^{4-}$, $\{\text{PW}_9\}^{9-}$, and $\{\text{Ni}_9\}^{16-}$ at $c_{SBMA} = 85.5 \text{ mM}$, $c_{LiCl} = 0.5 \text{ M}$, and $c_{e-(POM)}/c_{SBMA}$

= 100 %. **b)** Phase diagram of PSBMA-POM complex formation with different POMs at varied $c_{e^{-}\{POM\}}/c_{SBMA}$ but the same $c_{SBMA} = 85.5$ mM and $c_{LiCl} = 0.5$ M. Similar to the case of PSBMA- $\{W_{12}\}$ complex formation, distinct phases including solution (black squares), biphasic coacervate complex (red circles), and gel-like complex (blue triangles) are observed with different POM anions, despite varied lower and upper critical ratios of $c_{e^{-}\{POM\}}/c_{SBMA}$ for the onset of coacervate and gel-like complex/solution formation, respectively, which certainly warrants future study beyond the scope of this report.

3. Linear Rheological Characterization of PSBMA- $\{W_{12}\}$ Complexes.

To characterize the viscoelastic properties of PSBMA- $\{W_{12}\}$ complexes in aqueous solution, a stress-controlled rheometer (Malvern, Gemini HRnano) equipped with sample cells of different geometry, including a double gap fluid cell, a cone-and-plate fluid cell of 40 mm in diameter and 4° in cone angle, and a parallel-plate fluid cell with 20 mm in diameter, was employed. Due to the considerable change of the viscoelastic properties of PSBMA- $\{W_{12}\}$ complexes in different phases, a double gap fluid cell was used to characterize the dilute solution-like complex, while a cone-and-plate fluid cell was used to characterize the gel-like complex. As dense coacervate is highly viscous, a parallel-plate fluid cell was employed. When using the cone-and-plate or the parallel-plate fluid cell, a thin film of liquid paraffin (Sigma-Aldrich) was carefully applied to the menisci of the sample cell to minimize solvent evaporation and thereby ensure reliable measurements over a long time period of several hours, and the gap distance between the plates was set constant at 150 μ m for cone-and-plate and 1000 μ m for parallel plate. Oscillatory shear of constant strain, $\gamma = 2$ % and varied radian frequency, $\omega = 0.19$ - 22 rad/s was applied. The ω -dependent linear shear spectra of PSBMA- $\{W_{12}\}$ complexes at varied $c_{e^{-}\{W_{12}\}}/c_{SBMA}$ are shown in **Figure S3a** in comparison to the PSBMA- $\{W_{12}\}$ mixtures without added LiCl.

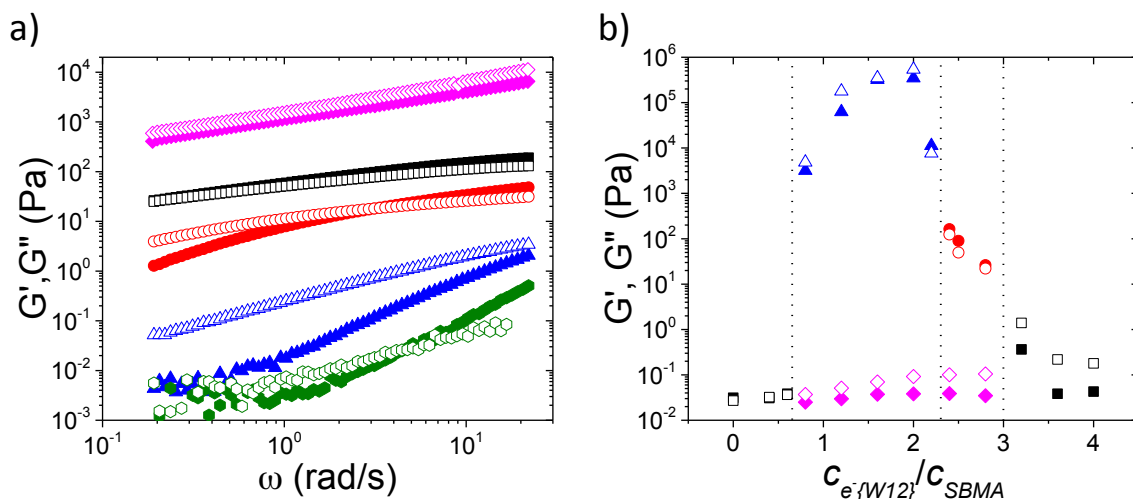


Figure S3. a) Measured linear elastic G' (solid symbols) and viscous moduli G'' (open symbols) of homogeneous PSBMA- $\{W_{12}\}$ complexes formed at $c_{e-\{W_{12}\}}/c_{SBMA} = 60\%$ (olive hexagons), 240 % (black squares), 280 % (red circles), and 320 % (blue triangles) at $c_{SBMA} = 85.5$ mM and $c_{LiCl} = 0.5$ M against ω in response to applied oscillatory shear of constant $\gamma = 2\%$. Also the linear viscoelastic spectrum of PSBMA- $\{W_{12}\}$ dense coacervate formed at $c_{e-\{W_{12}\}}/c_{SBMA} = 80\%$ (magenta diamonds) at the same c_{SBMA} and c_{LiCl} is obtained after the removal of dilute supernatant. **b)** Measured G' (solid symbols) and viscous moduli G'' (open symbols) of PSBMA- $\{W_{12}\}$ solution (black squares), dense coacervate (blue triangles), and gel-like complex (red circles) against $c_{e-\{W_{12}\}}/c_{SBMA} = 0-400\%$ at constant $c_{SBMA} = 85.5$ mM and $c_{LiCl} = 0.5$ M in response to applied oscillatory shear of constant $\gamma = 2\%$ and $\omega = 6.3$ rad/s. Shear moduli (magenta diamonds) of PSBMA- $\{W_{12}\}$ solution without added LiCl against $c_{e-\{W_{12}\}}/c_{SBMA} = 80-280\%$ at $c_{SBMA} = 85.5$ mM is also plotted for comparison.

As shown in **Figure S3b**, measured elastic, G' and viscous, G'' moduli of PSBMA- $\{W_{12}\}$ complexes at $\omega = 6.3$ rad/s are compared against $c_{e-\{W_{12}\}}/c_{SBMA}$. For PSBMA- $\{W_{12}\}$ mixture with added 0.5 M LiCl, the mixture at low $c_{e-\{W_{12}\}}/c_{SBMA} \leq 60\%$ is homogeneous and exhibits typical liquid-like viscoelastic behavior with $G'' > G'$. Measured G'' shows weak dependence on $c_{e-\{W_{12}\}}/c_{SBMA}$ similar to the viscoelastic behavior of homogeneous PSBMA- $\{W_{12}\}$ solution in the absence of LiCl. As increasing $c_{e-\{W_{12}\}}/c_{SBMA}$ from 80%-220%, liquid-liquid phase separation in the PSBMA- $\{W_{12}\}$ mixture with added 0.5 M LiCl, indicating the coacervate complex formation. Due to the instability of the biphasic coacervate complexes, in

this $c_{e-\{W_{12}\}}/c_{SBMA}$ range, we have focused on characterizing the dense coacervate after the removal of dilute supernatant by centrifugation. The dense PSBMA- $\{W_{12}\}$ coacervate is highly viscous and show the measured G'' and G' about 4-5 orders of magnitude higher than those of salt-free PSBMA- $\{W_{12}\}$ solution at the same $c_{e-\{W_{12}\}}/c_{SBMA}$, which in part due to enhanced polymer-POM network structure and in part due to higher PSBMA and $\{W_{12}\}$ concentration in the dense coacervate phase according to the TGA results as shown in **Figure 3**. As further increasing $c_{e-\{W_{12}\}}/c_{SBMA}$ to exceed 220%, the mixture exhibits homogeneous gel-like complex. Surprisingly, as increasing $c_{e-\{W_{12}\}}/c_{SBMA}$ from 240%-320%, measured G'' and G' decrease considerably. Additionally, a transition from gel-like complex to solution is observed with the transition from nearly overlapping shear moduli, $G'' \sim G'$, to the predominant viscous response, $G'' > G'$ at $c_{e-\{W_{12}\}}/c_{SBMA} = 300\%$. Hence, the drastic change of the linear viscoelastic behaviors of PSBMA- $\{W_{12}\}$ mixtures in LiCl aqueous solution clearly reflect the distinct phase transition from solution, biphasic coacervate complexes, to gel-like complex or solution with increased $c_{e-\{W_{12}\}}/c_{SBMA}$ as observed microscopically shown in **Figure 1**.

4. Supernatant Conductivity of Biphasic PSBMA- $\{W_{12}\}$ Complexes.

The conductivity of dilute supernatant of biphasic PSBMA- $\{W_{12}\}$ complex was determined by a conductivity meter (B-173, Horiba), in comparison to that of PSBMA-free aqueous solutions of the same LiCl and $\{W_{12}\}$ concentration.

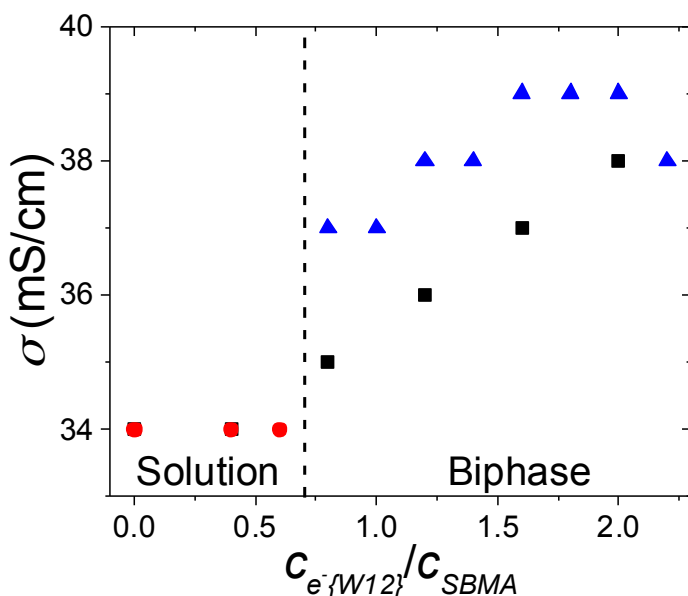


Figure S4. Measured conductivity of PSBMA- $\{W_{12}\}$ supernatant solutions (blue triangles) extracted from the coacervate complex formed at $c_{SBMA} = 85.5$ mM and $c_{LiCl} = 0.5$ M against $c_{e^{-}\{W_{12}\}}/c_{SBMA} = 80\text{--}220\%$, in comparison to the control of PSBMA- $\{W_{12}\}$ solution (red circles) formed at $c_{SBMA} = 85.5$ mM and $c_{LiCl} = 0.5$ M against $c_{e^{-}\{W_{12}\}}/c_{SBMA} = 0\text{--}60\%$ and PSBMA-free aqueous solutions (black symbols) of $c_{LiCl} = 0.5$ M and increased $\{W_{12}\}$ concentration from $c_{\{W_{12}\}} = 0\text{--}34.2$ mM.

5. Specific Ion Effect on PSBMA- $\{W_{12}\}$ Coacervate Complexation.

The specific ion effect on the phase diagram of PSBMA- $\{W_{12}\}$ complexes is investigated at the same ionic strength of 0.5 M. It is reported that different monovalent anions exhibit different binding affinity to PSBMA, resulting in varied PSBMA solubility in water by following the classic Hofmeister anion series: $SCN^{-} > NO_{3}^{-} > Cl^{-}$.⁵⁻⁷ As it is hypothesized that the PSBMA- $\{W_{12}\}$ coacervate formation is entropy driven by the displacement and release of simple anions near PSBMA with the stronger binding of multivalent $\{W_{12}\}$ to PSBMA, we speculate that simple anions with higher affinity to PSBMA could weaken the formation of PSBMA- $\{W_{12}\}$ coacervate. As shown in **Figure S5**, we have found that the coacervate phase is indeed narrowed by added SCN^{-} and NO_{3}^{-} in comparison to the case of added Cl^{-} , following the same Hofmeister

anion series: $\text{SCN}^- > \text{NO}_3^- > \text{Cl}^-$. The results strongly support the proposed mechanism of entropy-driven ion pairing for PSBMA-POM coacervate formation in salted aqueous solution.

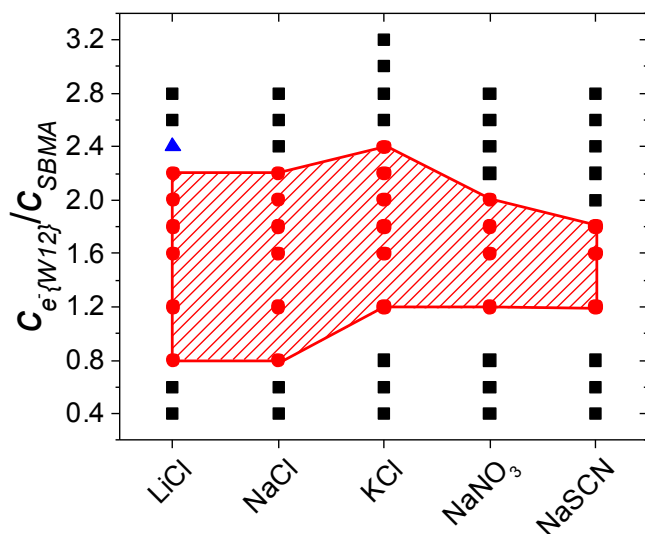


Figure S5. Specific salt effect on the phase diagram of PSBMA- $\{\text{W}_{12}\}$ complex formation at constant $c_{\text{SBMA}} = 85.5$ mM and $c_{\text{salt}} = 0.5$ M. For aqueous solutions added with different salt, the ionic strength is kept constant at 0.5 M.

6. Electrical Potential of Zwitterionic PSBMA in Aqueous Solution.

To examine how Cl^- and $\{\text{W}_{12}\}$ anions bind competitively with zwitterionic PSBMA in the aqueous mixture, we determine the electric potential of PSBMA in LiCl and $\{\text{W}_{12}\}$ added dilute aqueous solution by UV-vis spectroscopy. Zwitterionic PSBMA in aqueous solution is expected to be net charge neutral. However, as PSBMA tends to attract and bind with anions⁵⁻⁷, its electric potential in salt solution could become net negatively charged. And the anions with higher binding affinity could lead to increased charge negativity in measured electric potential of the polymer. In this work, we use a fluorophore, fluorescein, to determine local proton concentration in the vicinity to PSBMA in comparison to the bulk proton concentration by UV-Vis spectroscopy. To probe the local proton concentration in the vicinity of PSBMA, fluorescein is

copolymerized with SBMA, designated as f-PSBMA. We choose proton as the probing ion because it is the smallest and most detectable ion in aqueous solution with highest penetrability, fastest diffusivity, and extremely short dissociate time below nanosecond⁸.

The UV-Vis spectroscopic profile of fluorescein strongly depends on the solution pH. As shown in **Figure S6a**, the strongest and most pH-sensitive absorption peak, Abs_{500} of fluorescence is located at the wavelength of 500 nm, resulting from the protonation and deprotonation of the phenol group in fluorescein. The peak value of Abs_{500} decreases with decreasing pH⁹. The shape of all the Abs_{500} spectra of f-PSBMA is similar to that of free fluorescein, indicating similar pH-sensitivity and photophysical property of PSBMA-attached fluorophore. Accordingly, the peak values of Abs_{500} are plotted against solution pH for both free fluorescein and f-PSBMA in aqueous solutions of varied Cl^- and $\{W_{12}\}$ concentration as shown in Figure 4a, yielding the typical titration curve to determine the pKa of fluorescein in varied aqueous solutions.

The local proton concentration in the vicinity of f-PSBMA can be derived by comparison to the pH-dependent Abs_{500} profile of free fluorescein in the same salt condition as reference. The difference between local and bulk proton concentration, i.e. pH difference, can yield the electric potential. The Abs_{500} profiles of f-PSBMA shift to higher pH range than those of free fluorescein at the same salt concentration, suggesting negative electric potential of f-PSBMA. The finding of net negatively charged PSBMA in salted solution is consistent with previous reports that sulfobetaine tends to bind with anions^{5-7, 10, 11}. In comparison to the profile of f-PSBMA in 100 mM KCl solution, the Abs_{500} profiles of f-PSBMA in 12.5 mM $Na_6[H_2W_{12}O_{40}]$ solution shifts to further higher pH range, indicating further increased charge negativity of PSBMA in multivalent $\{W_{12}\}$. To quantify the local electric potential of PSBMA, the pH values

corresponding to the half upper plateau of Abs₅₀₀ profiles (dash lines in Figure 4a) for f-PSBAM and free fluorescein are determined as the local and bulk pH respectively, because they actually correspond to the pK_{a_f} and $pK_{a_{f-PSBMA}}$ of the phenol group for respective free fluorescein and f-PSBMA, where fluorescein exhibits the highest sensitivity to local proton concentration. Hence, by using modified Boltzmann Equation, the electric potential of PSBMA could be calculated by
$$\psi = \frac{k_B T (\text{pH}_{\text{local}} - \text{pH}_{\text{bulk}}) \ln 10}{e} = k_B T (pK_{a_f} - pK_{a_{f-PSBMA}}) \ln 10 / e.$$
 As such, the electric potential of f-PSBMA in aqueous solutions of varied Cl⁻ and {W₁₂} concentration can be obtained as reported in the manuscript.

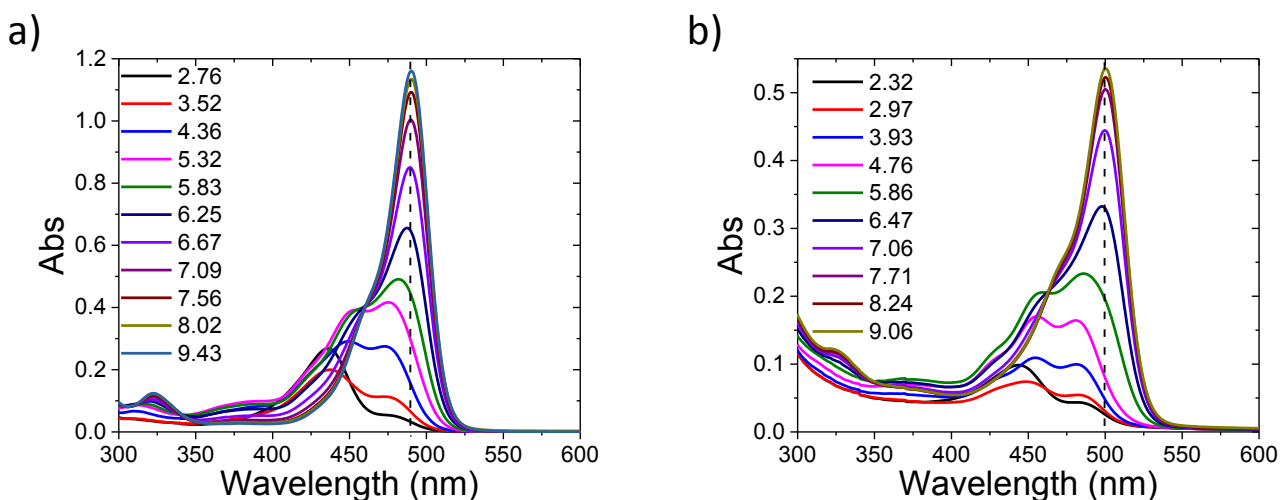


Figure S6. pH-dependent UV-Vis spectra of a) 10 μM free fluorescein and b) 10 g/L f-PSBMA in buffer solutions of varied pH from 2-10. The dash line indicates the location of primary UV-Vis absorbance peak, Abs₅₀₀, which shifts from 490 nm for the case of free fluorescein to 500 nm for f-PSBMA possibly due to local environment change.

7. Isothermal Titration Calorimetry Characterization of Mixing {W₁₂} with PSBMA-LiCl Aqueous Solution.

The enthalpy change during PSBMA- $\{W_{12}\}$ complexation is determined by isothermal titration calorimetry (ITC, Nano ITC, TA Instruments). Experimentally, 26 consecutive aliquots

of each 10 μL $\{\text{W}_{12}\}$ /LiCl mixed solution of $c_{\{\text{W}_{12}\}} = 60 \text{ mM}$ and $c_{\text{LiCl}} = 0.5 \text{ M}$ were injected into a 1.1 mL liquid cell filled with 950 μL PSBMA/LiCl mixed solution of $c_{\text{PSBMA}} = 6.84 \text{ mM}$ and $c_{\text{LiCl}} = 0.5 \text{ M}$. Subsequent injection of $\{\text{W}_{12}\}$ was carried out at a time interval of 400 s. A constant stirring speed of 250 rpm was maintained throughout the experiment to ensure sufficient mixing after each injection. As shown in **Figure S7**, enthalpy change upon mixing $\{\text{W}_{12}\}$ with PSBMA in LiCl solution is negligible, strongly supporting the entropy-driven ion pairing between PSBMA and $\{\text{W}_{12}\}$ for the formation of PSBMA- $\{\text{W}_{12}\}$ coacervates. It is also noted that the ITC data are not suitable for further data fitting possibly because the measured enthalpy change is too small.

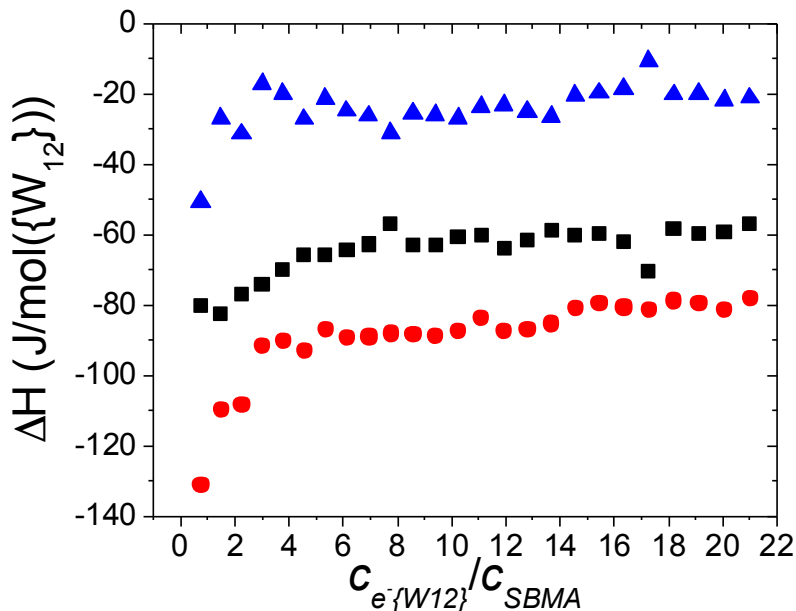


Figure S7. Measured enthalpy change (blue triangles) of added $\{\text{W}_{12}\}$ -LiCl solution to PSBMA-LiCl solution at the same LiCl concentration at 40 °C. The enthalpy change of injecting $\{\text{W}_{12}\}$ /LiCl to PSBMA/LiCl (red circles) is measured in comparison to the enthalpy change of injecting $\{\text{W}_{12}\}$ -LiCl solution to LiCl solution at the same concentrations (black squares).

References

1. Ishikawa-Ankerhold, H. C.; Ankerhold, R.; Drummen, G. P. C., Advanced Fluorescence Microscopy Techniques—FRAP, FLIP, FLAP, FRET and FLIM. *Molecules* **2012**, *17*, 4047.
2. Reits, E. A. J.; Neefjes, J. J., From fixed to FRAP: measuring protein mobility and activity in living cells. *Nat. Cell. Biol.* **2001**, *3*, E145-E147.
3. Téazéa, A.; Hervéa, G.; Finke, R. G.; Lyon, D. K., α -, β -, and γ -Dodecatungstosilicic Acids: Isomers and Related Lacunary Compounds. In *Inorg. Synth.*, John Wiley & Sons, Inc.: 2007; pp 85-96.
4. Clemente-Juan, J. M.; Coronado, E.; Galán-Mascarós, J. R.; Gómez-García, C. J., Increasing the Nuclearity of Magnetic Polyoxometalates. Syntheses, Structures, and Magnetic Properties of Salts of the Heteropoly Complexes $[\text{Ni}_3(\text{H}_2\text{O})_3(\text{PW}_{10}\text{O}_{39})\text{H}_2\text{O}]_7^-$, $[\text{Ni}_4(\text{H}_2\text{O})_2(\text{PW}_9\text{O}_{34})_2]_{10}^-$, and $[\text{Ni}_9(\text{OH})_3(\text{H}_2\text{O})_6(\text{HPO}_4)_2(\text{PW}_9\text{O}_{34})_3]_{16}$. *Inorg. Chem.* **1999**, *38*, 55-63.
5. Wang, T.; Kou, R.; Liu, H.; Liu, L.; Zhang, G.; Liu, G., Anion Specificity of Polyzwitterionic Brushes with Different Carbon Spacer Lengths and Its Application for Controlling Protein Adsorption. *Langmuir* **2016**, *32*, 2698-2707.
6. Wang, T.; Wang, X.; Long, Y.; Liu, G.; Zhang, G., Ion-Specific Conformational Behavior of Polyzwitterionic Brushes: Exploiting It for Protein Adsorption/Desorption Control. *Langmuir* **2013**, *29*, 6588-6596.
7. Wang, F.; Yang, J.; Zhao, J., Understanding Anti-polyelectrolyte Behavior of a Well-defined Polyzwitterion at the Single-chain Level. *Polym. Int.* **2015**, *64*, 999-1005.
8. Gutman, M.; Nachliel, E., The Dynamic Aspects of Proton Transfer Processes. *Biochim. Biophys. Acta, Bioenerg.* **1990**, *1015*, 391-414.
9. Sjöback, R.; Nygren, J.; Kubista, M., Absorption and Fluorescence Properties of Fluorescein. *Spectrochim. Acta, Part A* **1995**, *51*, L7-L21.
10. Santos, D. P.; Longo, R. L., Molecular Dynamics Simulations of Specific Anion Adsorption on Sulfobetaine (SB3-14) Micelles. *J. Phys. Chem. B* **2016**, *120*, 2771-2780.
11. Pedro, J. A.; Mora, J. R.; Silva, M.; Fiedler, H. D.; Bunton, C. A.; Nome, F., Surface Charge of Zwitterionic Sulfobetaine Micelles with 2-Naphthol as a Fluorescent Probe. *Langmuir* **2012**, *28*, 17623-17631.